A plane-strain hydraulic fracture driven by a shear-thinning Carreau fluid

Lucas Pereira and Brice Lecampion[1]

[1]Geo-Energy Lab - Gaznat chair on Geo-Energy - EPFL, Lausanne, Switzerland

March 22, 2021

Abstract

We study the propagation of a plane-strain hydraulic fracture driven by a shear thinning fluid following a Carreau rheology. We restrict to the impermeable medium case and quantify in details the impact on fracture growth of the shear-thinning properties of the fluid between the low and high shear-rates Newtonian limits. We derive several dimensionless numbers governing the evolution of the solution. The propagation notably depends on the ratio between the two limiting viscosities, the fluid shear-thinning index, a dimensionless fracture toughness and a characteristic time-scale capturing the instant at which the fluid inside the fracture reaches the low-shear rate Newtonian plateau. We solve the problem numerically using Gauss-Chebyshev methods for the spatial discretization of the coupled hydro-mechanical problem and a fully implicit time integration scheme. The solution evolves from an early time self-similar solution equals to the Newtonian one for the large-shear rate viscosity to a late time self-similar solution equals to the low-shear rate Newtonian solution. The transition period (corresponding to the shear thinning part of the rheology) exhibits features similar to the power law rheology, albeit quantitatively different. Comparisons of hydraulic fracture growth predictions obtained with a power-law model confirm its inadequacy for realistic fluids used in practice compared to the more physical Carreau rheology: the Newtonian plateau at high and low shear rates cannot be neglected.

Key words: *fluid-driven cracks, complex fluids, Gauss-Chebyshev quadrature*

1 Introduction

The type of fluids used during hydraulic fracturing operations is the main component that can be engineered notably in relation to their capacities to carry propping agents, minimize plugging of the fracture faces and ensuring minimal pumping energy. Over the years, a variety of proprietary fluid formulation have therefore been developed by pumping services companies from dilute polymer solutions (slickwater), linear and cross-linked gels to viscoelastic surfactants (micellar fluids). We refer to Barbati *et al.* [1] for a review. Most of these fluids exhibit a non-linear shear-thinning rheological behaviour: their tangent viscosity decreases with increasing shear rate / shear stress. More precisely, these fluids exhibit a Newtonian plateau at low shear rate where their viscosity is maximum and starts to shear thin for value of shear rate larger than a critical value $\dot{\gamma}_c$. At very large shear rate, the viscosity tends to the Newtonian viscosity of the base solvent used (see Fig. 1).

How such non-linear rheological fluid behavior impacts the growth of a hydraulic fracture is an important question in practice. A large number of work in the hydraulic fracturing literature have approximated the shear-thinning behavior by a power-law rheology (also sometimes referred to as the Ostwald–de Waele model). Such a power-law variation clearly over-estimates the fluid tangent viscosity at low shear rates and under-predicts it at large shear rates (see Fig. 1). Nevertheless,
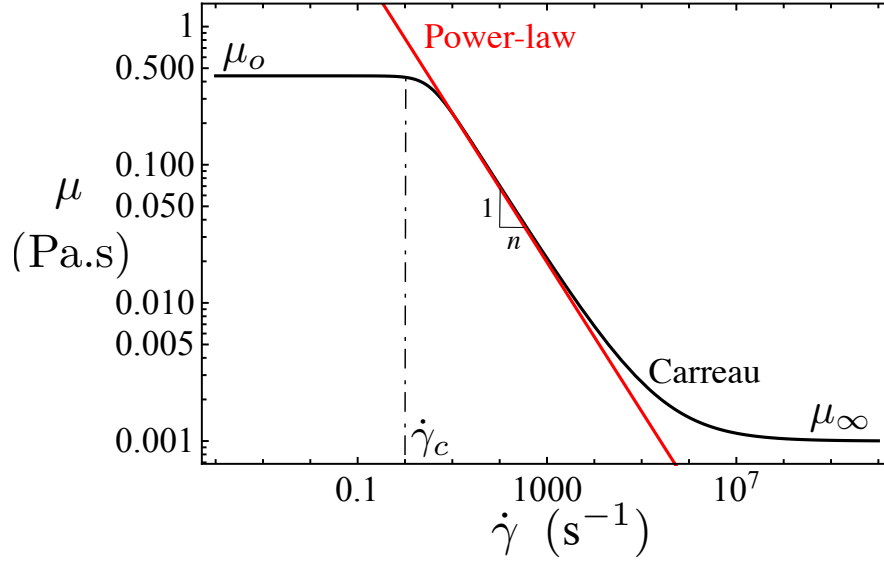
Figure 1: Example of the evolution of the viscosity as function of shear rate for the Carreau (black line) and power law rheological models (red line). Case representative of a Hydroxypropylguar (HPG) fluid - see e.g. [13, 18] for other examples.

thanks to the simple expression of the power-law model, the lubrication relation in a thin fracture between flow rate and the fluid pressure gradient is analytical. Semi-analytical reference solutions for a hydraulic fracture driven by a power-law fluid have thus been obtained for a plane-strain geometry [2, 3],complementing solutions already available for the case of Newtonian fluids (see [4, 5, 6] for a comprehensive list of references). The solution for a steadily moving semi-infinite fluid driven crack has also been derived for a power-law fluid [7, 8]. The power-law rheology despite its short-comings is implemented in a large number of computer codes [6, 9].

In this article, we investigate in details how the precise evolution from the low shear-rate to the large shear rate Newtonian plateau impacts the growth of a finite plane-strain hydraulic fracture. To do so, we use the Carreau rheological model [10] which captures well the shear-thinning behavior from low to high shear rates (see Fig. 1). Similar results would be obtained with similar rheological models [11]. It is worth noting that a semi-analytical solution for the lubrication flow of a Carreau fluid between two parallel plates exist (in the form of a non-linear scalar equation for the wall shear-stress) and will be subsequently used [12]. In what follows, we extend the work of Moukhtari and Lecampion [13] who studied the asymptotic case of a steadily moving semi-infinite fracture. Very recently, as we finalize this work, the propagation of a plane-strain hydraulic fracture driven by a truncated power-law rheology (which is an approximation of the Carreau model [14]) has been investigated numerically [15]. Our analysis using the complete Carreau rheology goes in more details regarding the different regimes of the solution. After discussing in details the structure of the hydraulic fracture propagation solution at the light of a scaling analysis, we present an efficient numerical scheme for the case of a finite plane-strain fracture based on Gauss-Chebyshev quadrature and barycentric differentiation / interpolation techniques [16, 17]. We then notably compare the results obtained with Carreau rheology with the power-law model.

2 Governing equations

We consider the propagation of a finite hydraulic fracture under plane-strain condition driven by the injection of a complex shear-thinning fluid modelled by a Carreau rheology. The fracture is fully filled by the non-linear fluid. The presence of a fluid lag is neglected which is a reasonable

assumptions when the in-situ confining stress σ_o is sufficiently large (see [13, 19] for a detailed discussion for Newtonian and Carreau fluids respectively). We further assume that the material is impermeable and isotropic linear elastic. The fluid is injected from a point source at the fracture center under a constant rate Q_o.

In line with previous contributions [4, 20], for sake of clarity, we use the following set of material parameters:

$$K' = \sqrt{\frac{32}{\pi}} K_{Ic} \quad E' = \frac{E}{1 - \nu^2} \quad \mu_o' = 12\mu_o \tag{1}$$

where K_{Ic} denotes the solid fracture toughness, E and ν the solid elastic Young's modulus and Poisson's ratio and μ_o is the fluid low shear viscosity.

2.1 Linear elastic fracture mechanics

In the case of a pure tensile mode I fracture growing symmetrically under plane-strain condition, the quasi-static elastic deformation of the material reduces to the following normal traction boundary integral equation between the net pressure loading $p(x)$ and the fracture opening $w(x)$ [21]:

$$\frac{E'}{4\pi} \int_{-\ell(t)}^{\ell(t)} \frac{\partial w}{\partial s} \frac{\mathrm{d}s}{x - s} = p(x, t) \tag{2}$$

where the net pressure loading $p(x, t) = p_f(x, t) - \sigma_o$ is the fluid pressure p_f in excess of σ_o the minimum in-situ confining stress acting perpendicular to the fracture plane. Due to the uniformity of the medium and in-situ stress field, the fracture grows symmetrically from a point source, and $\ell(t)$ denotes its half-length.

We assume quasi-static co-planar fracture growth under pure mode I such that the Griffith propagation criteria reduces to the equality of the mode I stress intensity factor with the material fracture toughness K_{Ic} (see [22] for example). Such a propagation condition notably results in the $1/2$ asymptote for the width near the fracture tip

$$w(x) = \frac{K'}{E'} (\ell - x)^{\frac{1}{2}} \qquad (\ell - x) \ll \ell \tag{3}$$

2.2 Lubrication flow

Recognizing that the length of the fracture is much longer than its width, the fluid flow is well approximated by the lubrication theory [23]. In the absence of any fracturing fluid leaking off from the fracture to surrounding medium, for an incompressible fluid, the width-averaged fluid mass conservation reduces to:

$$\frac{\partial w(x, t)}{\partial t} + \frac{\partial q(x, t)}{\partial x} = 0 \tag{4}$$

where $q = w \times V$ denotes the local fluid flux, and V the width-averaged fluid velocity.

We use the Carreau rheological model [10] to capture the shear-thinning behaviour of the fracturing fluid. This model expresses the tangent viscosity μ in simple shear as a function of the shear-rate $\dot{\gamma}$ as:

$$\mu = \mu_\infty + (\mu_o - \mu_\infty) \times \left(1 + (\dot{\gamma}/\dot{\gamma}_c)^2\right)^{(n-1)/2} \tag{5}$$

where μ_o and μ_∞ are respectively the viscosity at low and large shear-rates (the large shear-rate visscosity is typically equal to the solvent viscosity), n the fluid shear-thinning index and $\dot{\gamma}_c$ the shear rate at which the fluid starts to shear-thin.

For laminar flow under lubrication conditions ($w \ll \ell$), the width average of the balance of momentum yields for a Carreau fluid the following Poiseuille's like relation between the between the local fluid flux and pressure gradient [12]:

$$q(x, t) = -\frac{w^3(x, t)}{\mu_o' \times \Gamma\left(\tau_w/(\mu_o \dot{\gamma}_c), \mu_\infty/\mu_o, n\right)} \frac{\partial p_f(x, t)}{\partial x} \tag{6}$$
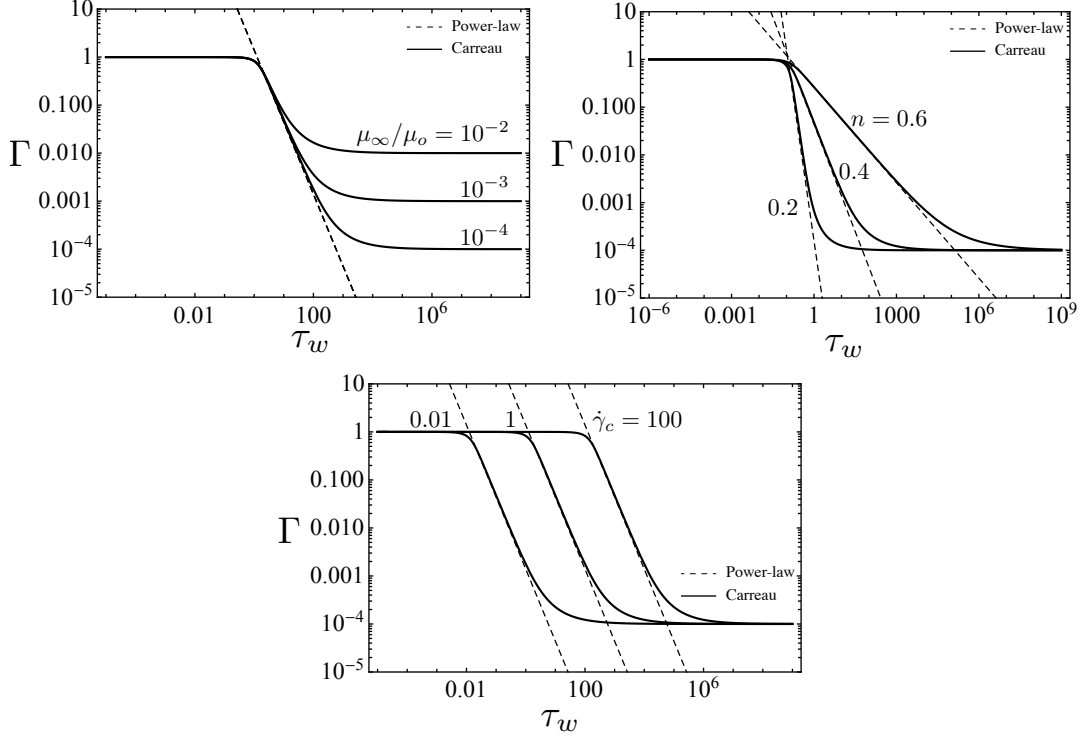
3

Figure 2: Dimensionless tangent geometric viscosity Γ as a function of the wall shear stress in plate parallel flow for the Carreau (solid lines) and Power-law rheolog (dashed lines): (a) effect of the viscosity ratio $r = \mu_\infty/\mu_o$ (for $\dot{\gamma}_c = 1$ and $n = 0.4$), (b) the fluid index n (for $\mu_\infty/\mu_o = 10^{-4}$ and $\dot{\gamma}_c = 1$), (c) the critical shear rate $\dot{\gamma}_c$ ($\mu_\infty/\mu_o = 10^{-4}$ and $n = 0.4$).

where Γ is a dimensionless apparent width-averaged geometric factor for parallel plates-like flow of a Carreau fluid. We will also refer it as a dimensionless tangent viscosity for short. It is a non-linear (implicit) function of the fluid shear stress at the walls of the fracture

$$\tau_w = \frac{w}{2}\left|\frac{\partial p_f}{\partial x}\right|. \tag{7}$$

It also depends on the ratio between the high and low shear rate viscosities μ_∞/μ_o, the critical shear rate at which the fluid starts to shear thin $\dot{\gamma}_c$ and the shear-thinning power-law index n. This dimensionless apparent geometric viscosity Γ requires the numerical solution of a non-linear scalar equation for a given value of wall shear stress τ_w (see [12, 13] for details and appendix A for summary).

We display in Fig. 2 the evolution of Γ as function of the wall-shear stress for different values of the shear thinning index, viscosity ratio and $\dot{\gamma}_c$. We also display on the same figure, the corresponding power-law model expression for Γ (see appendix B for details). Similarly to simple shear, the power-law model matches the Carreau only for an intermediate range of wall shear-stress corresponding to the shear-thinning region similarly to the case of simple shear flow (see Fig. 1).

2.3   Boundary conditions

The growing plane-strain fracture has two symmetric wings and the fluid is injected at $x = 0$ at a constant rate. In addition, in the absence of a fluid lag, the width and fluid flux vanish to zero at the fracture tip [24]:

$$q(0,t) = Q_o/2 \qquad q(\ell) = 0 \qquad w(\ell) = 0 \tag{8}$$

4

2.4 Global volume conservation

The integration of the continuity equation (4) taking into account the boundary and symmetry conditions yields the following global volume conservation

$$2 \int_0^{\ell(t)} w(x,t) \, \mathrm{d}x = Q_o t \tag{9}$$

3 Scaling and structure of the solution

3.1 Scaling

Following previous contributions on plane-strain fracture driven by a Newtonian fluid [25, 26], for such a moving boundary fracture problem, it is natural to introduce a characteristic length $L(t)$ and a characteristic width as $\varepsilon(t)L(t)$ where $\varepsilon(t)$ is a small dimensionless number reflecting the fact that $w \ll \ell$. Similarly, the net pressure p is much smaller than typical value of the elastic modulus, such that $\varepsilon(t)E'$ provides a characteristic pressure scale. As a result, introducing the scaled spatial coordinate $\xi = x/\ell(t)$, we scale the fracture length, width and net pressure as

$$\ell(t) = \gamma(P(t))L(t) \qquad w(x,t) = \varepsilon(t)L(t)\Omega(\xi, P(t)), \qquad p(x,t) = \varepsilon(t)E'\Pi(\xi, P(t)) \tag{10}$$

where γ, Ω and Π are the dimensionless length, width and net pressure while P(t) denotes additional dimensionless parameters on which the solution depends. Introducing these scales in the global volume balance gives the following dimensionless group

$$\mathcal{G}_v = \frac{Q_o t}{L^2 \varepsilon}, \tag{11}$$

which is the ratio between the injected volume and characteristic fracture volume. In the absence of fluid leak-off (impermeable medium case), we must have $\mathcal{G}_v = 1$, in other words $\varepsilon = Q_o t/L^2$. The fracture propagation condition and Poiseuille's like relation provides two additional dimensionless groups

$$\mathcal{G}_k = \frac{K'}{\varepsilon E' L^{\frac{1}{2}}} \qquad \mathcal{G}_m = \frac{\mu'_o}{\varepsilon^3 E' t} \tag{12}$$

In addition, for a Carreau fluid, the dimensionless apparent geometric viscosity Γ can be re-written as function of the viscosity ratio μ_∞/μ_o, the shear thinning index n (dimensionless), and a dimensionless fluid shear stress at the wall

$$\tau_w/(\mu_o \dot{\gamma}_c) = \mathcal{G}_\alpha \frac{\Omega}{2} \frac{1}{\gamma} \left| \frac{\partial \Pi}{\partial \xi} \right| \tag{13}$$

where $\mathcal{G}_\alpha$ is the ratio between the characteristic wall shear stress $\varepsilon^2 E'$ (obtained by introducing the scaling (10) in Eq. (7)) and the fluid shear stress at the onset of shear thinning $\mu_o \dot{\gamma}_c$:

$$\mathcal{G}_\alpha = \frac{\varepsilon^2 E'}{\mu_o \dot{\gamma}_c} = 12 \frac{\varepsilon^2 E'}{\mu'_o \dot{\gamma}_c} \tag{14}$$

Newtonian case

For a Newtonian fluid, two scalings are possible in relation to the dominance of viscosity or toughness dissipation. If fluid viscous dissipation dominates, setting the dimensionless group associated with viscous $\mathcal{G}_m$ to unity, one obtains (using a subscript m for this viscosity scaling):

$$\varepsilon_m(t) = \left(\frac{\mu'_o}{E't} \right)^{1/3} \qquad L_m(t) = \frac{E'^{1/6} Q_o^{1/2} t^{2/3}}{\mu'^{1/6}_o} \tag{15}$$

and the solution depends on a single dimensionless toughness $\mathcal{K} = \mathcal{G}_k$ which is independent of time:

$$\mathcal{G}_k = \mathcal{K} = K' \left(\frac{1}{E'^3 Q_o \mu'_o} \right)^{1/4} \tag{16}$$

Similarly, if fracture toughness dominates over viscous dissipation, a toughness scaling (subscript k) is obtained (by setting $\mathcal{G}_k$ to unity):

$$\varepsilon_k = \left(\frac{K'^4}{E'^4 Q_o t} \right)^{1/3} \qquad L_k = \left(\frac{E' Q_o t}{K'} \right)^{2/3} \tag{17}$$

and the solution depends on a dimensionless viscosity $\mathcal{G}_m = \mathcal{M}$ which is directly related to the dimensionless toughness

$$\mathcal{M} = \mathcal{G}_m = \mathcal{M} = \frac{E'^3 Q_o \mu'_o}{K'^4} = \mathcal{K}^{-4} \tag{18}$$

These two scalings are of course related as $\varepsilon_k^{3/4}/\varepsilon_m^{3/4} = L_m^{3/2}/L_k^{3/2} = \mathcal{K}$ (see e.g. [4] for details).

Solutions (and first order expansions) for small and large dimensionless toughness have been derived [4, 25, 26]. The growth solution is viscosity dominated for $\mathcal{K} \lesssim 1.3$, and purely toughness dominated (with little to no pressure drop) for $\mathcal{K} \gtrsim 3.7$ - as discussed in [27].

Carreau fluid

For a shear-thinning fluid, the dimensionless apparent geometric viscosity Γ introduces additional dependence of the solution upon n, the ratio μ_∞/μ_o but also on the dimensionless shear stress ratio $\mathcal{G}_\alpha$ (14) which enters the definition of the dimensionless shear stress (13). In the viscosity dominated scaling (defined above using the low-shear rate viscosity μ_o), we obtain

$$\mathcal{G}_\alpha = \alpha_m = 12 \left(\frac{E'}{t^2 \dot{\gamma}_c^3 \mu'_o} \right)^{1/3} . \tag{19}$$

The characteristic fluid shear stress at the wall $\varepsilon^2 E'$ decreases with time. At early time, the fluid shear stress will be much larger than the one at which the fluid starts to shear thin. As a result, the flow will be governed by the large shear rate /stress viscosity viscosity μ_∞ at early time, and will become dependent on the low shear rate viscosity when $\mathcal{G}_\alpha = 1$, which defines a characteristic time-scale

$$t_{m_\infty m_o} = 12^{3/2} \frac{E'^{1/2}}{\mu_o'^{1/2} \dot{\gamma}_c^{3/2}} \tag{20}$$

for the transition from a high shear rate dominated regime when $t \ll t_{m_\infty m_o}$ (at early time when the fracture velocity and as a result the fluid shear rate is large) to the low-shear rate dominated regime for $t \gg t_{m_\infty m_o}$.

Similarly, in the toughness dominated scaling, in addition to n and μ_∞/μ_o, the solution depends on the following dimensionless shear stress ratio $\mathcal{G}_\alpha = \alpha_k$

$$\alpha_k = \frac{12}{\dot{\gamma}_c \mu_o} \frac{K'^{8/3}}{E'^{5/3} Q_o^{2/3} t^{2/3}} = \mathcal{K}^{8/3} \times \alpha_m \tag{21}$$

and $\alpha_m/\alpha_k = \mathcal{M}^{2/3} = \mathcal{K}^{-8/3}$. In what follows, we mostly use the viscosity scaling to develop a numerical solver and discuss our results.

3.2 Structure of the solution

We have seen that at early time ($t \ll t_{m_\infty m_o}$) the characteristic fluid shear stress at the wall $\varepsilon^2 E'$ is much larger than the one at which the fluid starts to shear thin ($\mu_o \dot{\gamma}_c$): $\alpha_m \ll 1$ for small time. This introduces a characteristic time-scale $t_{m_\infty m_o}$ in the propagation solution which in additions
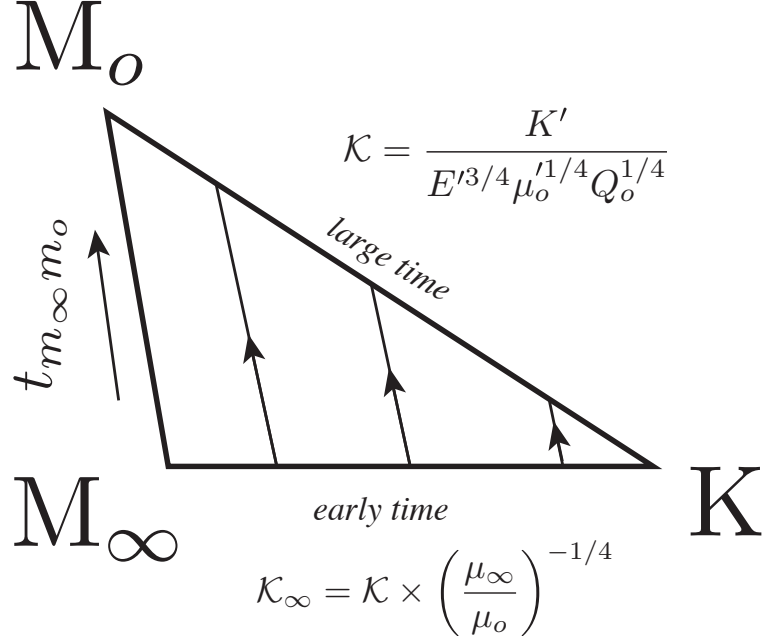
Figure 3: Schematic propagation diagram for a plane-strain HF driven by a Carreau fluid. The growth evolves from an early time edge ($t \ll t_{m_\infty m_o}$) where fluid dissipation is governed by the large shear rate plateau (and the solution corresponds to the Newtonian one with a dimensionless toughness $\mathcal{K}_\infty$ defined with μ_∞) to a large time edge ($t \gg t_{m_\infty m_o}$) where it is controlled by the low shear rate plateau (and the solution corresponds to the Newtonian one with a dimensionless toughness $\mathcal{K}$ defined with μ_o). The transition occurs over a the characteristic time-scale $t_{m_\infty m_o}$. Besides the dimensionless time $t/t_{m_\infty m_o}$, the solution depends on a dimensionless toughness $\mathcal{K}$, the viscosity ratio μ_∞/μ_o and power-law index n. The propagation is fully toughness dominated (with no effect of the fluid rheology) for dimensionless toughness $\mathcal{K} \gtrsim 3.7$ [27].

also depends on the usual (time-independent) dimensionless toughness $\mathcal{K}$ (16) for a plane-strain hydraulic fracture, the fluid shear-thinning index n and high to low shear rate viscosities ratio μ_∞/μ_o.

It appears clearly that at early time ($t \ll t_{m_\infty m_o}$), the large shear rate viscosity μ_∞ governs the fluid dissipation. The fluid is completely shear-thinned such that n, and μ_o do not influence the growth solution. As a result, the solution depends solely on the plane-strain HF dimensionless toughness defined using *the large shear rate viscosity* μ_∞, that we may denote $\mathcal{K}_\infty$ which is simply related to $\mathcal{K}$ (defined with μ_o):

$$\mathcal{K}_\infty = \mathcal{K} \times \left(\frac{\mu_\infty}{\mu_o}\right)^{-1/4} \tag{22}$$

As the time evolves, the shear-thinning behaviour of the fluid will enter into play, and finally at large time ($t \gg t_{m_\infty m_o}$) the fluid viscous dissipation is solely governed by the low shear rate plateau (μ_o). The growth solution is then a sole function of the dimensionless toughness $\mathcal{K}$ (defined with μ_o).

In addition, we see that as $\mu_\infty/\mu_o < 1$, if the dimensionless toughness $\mathcal{K}$ is larger than ~ 3.7 such that the growth is toughness dominated at large time, it will also necessarily be toughness dominated at early time. In other words, the viscous dissipation is always negligible: the growth will always follow the toughness dominated solution and the details of the fluid rheology have no impact on growth.

We therefore can schematically summarize the propagation via a triangular diagram with three vertices (see Fig. 3): K for a solely toughness dominated growth, M_∞ for viscosity dom-

inated growth with the large shear rate viscosity μ_∞, and M_o for viscosity dominated growth with the low shear rate viscosity μ_o. The solution evolves from the $M_\infty K$ edge at early time governed by the dimensionless toughness $\mathcal{K}_\infty$ toward the $M_o K$ edge at large time over a transition time-scale defined by $t_{m_\infty m_o}$. The shear-thinning index n will likely only influence the transition between the early and late time solutions.

Before proceeding to the complete numerical solution, it is interesting to grasp some order of magnitudes. Using a range of realistic values for both the fluid parameters ($\mu_o \in [0.5 - 100]$Pa.s, $\dot{\gamma}_c \in [0.1 - 30]1/$s) and solid elastic properties ($E' \in [2 - 60]$GPa), we see that the transition time-scale can vary between 200 seconds (soft rocks/viscous fluid) up to 10^8 seconds (stiff rocks/low viscosity). Depending on the injection rate and fracture toughness, the dimensionless toughness $\mathcal{K}$ can vary in a large range $[0.01 - 5]$ (see [27]). Note that μ_∞ is the solvent viscosity - typically water - such that $\mu_o/\mu_\infty \in [10^{-5} - 10^{-2}]$ and as a result $\mathcal{K}_\infty/\mathcal{K} \in [0.05 - 0.3]$. It thus possible that the propagation regime at early time is toughness dominated ($\mathcal{K}_\infty > 3.7$) and viscous dominated at large time ($\mathcal{K} < 1.3$)..

4   Numerical solution

In view of the previously discussed scaling of the solution, it is natural to scale the time t with the transition time-scale $t_{m_\infty m_o}$ and use a time-based scaling adapted from the viscosity scaling with $\tau = t/t_{m_\infty m_o}$ as the dimensionless time. We use time-independent characteristic length, width and pressure scales:

$$\overline{L}_m = L_m(t_{m_\infty m_o}) = \frac{12\sqrt{E'Q_o}}{\dot{\gamma}_c\sqrt{\mu_o'}} \qquad \overline{\varepsilon}_m = \varepsilon_m(t_{m_\infty m_o}) = \frac{\sqrt{\mu_o'\dot{\gamma}_c}}{2\sqrt{3}\sqrt{E'}} \tag{23}$$

The dimensionless shear stress ratio $\alpha_m = \alpha$ now simplifies to $\alpha_m = \tau^{-2/3}$. Emphasizing the dependence on the different dimensionless parameters, we can rewrite the length, width and net pressure in that time-based viscosity scaling as:

$$w = \overline{\varepsilon}_m\overline{L}_m\Omega(\xi,\tau,\mathcal{K},n,\mu_\infty/\mu_o) \qquad p = \overline{\varepsilon}_m E'\Pi(\xi,\tau,\mathcal{K},n,\mu_\infty/\mu_o) \qquad \ell = \overline{L}_m\gamma(\tau,\mathcal{K},n,\mu_\infty/\mu_o) \tag{24}$$

Note that $\overline{W}_m = \overline{\varepsilon}\overline{L}_m$ and $\overline{P}_m = \overline{\varepsilon}E'$ will be used to denote the characteristic width and net pressure scales. There is obviously a correspondence between this numerical scaling and the viscosity scaling:

$$\gamma = \tau^{\frac{2}{3}}\gamma_m \qquad \Omega = \tau^{\frac{1}{3}}\Omega_m \qquad \Pi = \tau^{-\frac{1}{3}}\Pi_m \tag{25}$$

where γ_m, Ω_m, Π_m correspond to the dimensionless quantities in the M viscosity scaling.

4.1   Dimensionless governing equations

In the moving frame of reference defined by $\xi = x/\ell(t)$, taking into account the convective derivative, the governing equations in the previous scaling (23)-(24) reduces to the following dimensionless system.

- Elasticity:

$$\frac{1}{4\pi\gamma}\int_{-1}^{1}\frac{\partial\Omega(\xi',\tau)}{\partial\xi'}\frac{d\xi'}{\xi - \xi'} = \Pi(\xi,\tau) \tag{26}$$

- Propagation condition:

$$\Omega = \mathcal{K}\gamma^{\frac{1}{2}}(1 - \xi)^{\frac{1}{2}} \qquad \text{for} \qquad (1 - \xi) << 1 \tag{27}$$

- Global volume balance:

$$2\gamma\int_0^1\Omega d\xi = \tau \tag{28}$$

- Reynolds equation (combining continuity (4) and the generalized Poiseuille (6) equations):

$$\frac{\partial \Omega}{\partial \tau} - \xi \frac{1}{\gamma} \frac{d\gamma}{d\tau} \frac{\partial \Omega}{\partial \xi} = \frac{1}{\gamma^2} \frac{\partial}{\partial \xi} \left(\frac{\Omega^3}{\Gamma(\tilde{\tau}_w, \mu_\infty/\mu_o, n)} \frac{\partial \Pi}{\partial \xi} \right) \tag{29}$$

with $\tilde{\tau}_w = \tau_w/(\mu_o \dot{\gamma}_c) = \alpha_m \Omega/2 \left| \frac{\partial \Pi}{\partial \xi} \right|$ the dimensionless fluid shear stress at the fracture walls (13), with $\alpha_m = \tau^{-2/3}$.

- The solution for the uni-dimensional pressure-driven flow of a Carreau fluid between parallel plates [12] can be expressed in this scaling as:

$$\Gamma(\tilde{\tau}_w, \mu_\infty/\mu_o, n) = \frac{\tilde{\tau}_w^3}{3I(\dot{\gamma}_w/\dot{\gamma}_c, \mu_\infty/\mu_o, n)} \tag{30}$$

where I is an analytical function obtained by Sochi [12] (see appendix A for its expression in dimensional form). For a given value of dimensionless shear stress at the wall the previous equation can be easily solved numerically for the corresponding dimensionless wall shear rate $(\dot{\gamma}_w/\dot{\gamma}_c)$ using a root-finding scheme. It thus easy to tabulate this tangent dimensionless viscosity as function of the dimensionless shear-stress for given values of the rheological parameters. As the dimensionless shear stress directly depends on dimensionless time $(\propto \tau^{-2/3})$, we tabulate such a function at every time step. The computational cost is minimal. Note that a complete interpolation over the whole range of n, μ_∞/μ_o and $\dot{\gamma}_w/\dot{\gamma}_c$ is also possible. The evolution of this tangent viscosity as a function of the wall shear stress $(\tau_w \tilde{\tau}_w \times (\mu_o \dot{\gamma}_c))$, and the impact of the different rheological parameters $(n, \mu_\infty/\mu_o, \dot{\gamma}_c)$ can be grasped on Fig. 2 .

The evolution of the dimensionless tangent geometric viscosity Γ will impact HF growth significantly. Indeed, the viscosity being defined locally as function of the dimensionless shear stress, we expect that the shear stress at the tip of the fracture will be larger than in the rest of the crack (due to the pressure gradient that increase at the tip), resulting in a region where the fluid will shear thin. As $\alpha_m = \tau^{-2/3}$ decrease with time, we also expect that the region where the flow is governed by the large shear rate viscosity μ_∞ will shrink and disappear as the low-shear rate Newtonian plateau extends further for large α.

4.2 Numerical algorithm

The spatial discretization is performed using a Gauss-Chebyshev quadrature and barycentric differentiation thus transforming the governing equations into a system of non-linear ordinary differential equations (ODEs) in time. Following Gauss-Chebyshev techniques for fracture problem [16, 28], we write the dislocation density as a product of a weight function $\omega(s) = 1/\sqrt{1-s^2}$ containing the proper tip singularity and a non-singular function $F(s)$:

$$\frac{\partial \Omega(s, \tau)}{\partial s} = \omega(s) \times F(s, \tau) \tag{31}$$

and use $F(s, \tau)$ at quadrature points (s-points) and the dimensionless fracture length $\gamma(\tau)$ as the main unknowns of the system. We notably combine barycentric differentiation techniques with Gauss-Chebyshev quadrature following the techniques described in [16] to obtain a system of ODEs. Pending the presence of the non-linear viscosity, the method is similar to the one described in [17] for the finite plane-strain and radial hydraulic fracture cases driven by a Newtonian fluid. The details of the different operators are given in appendix C.

We use a fully implicit time-integration scheme due to the stiff behavior of the resulting system. The final non-linear system over a given time-step $(\tau^{n+1} = \tau^n + \Delta\tau)$ is given in appendix C.
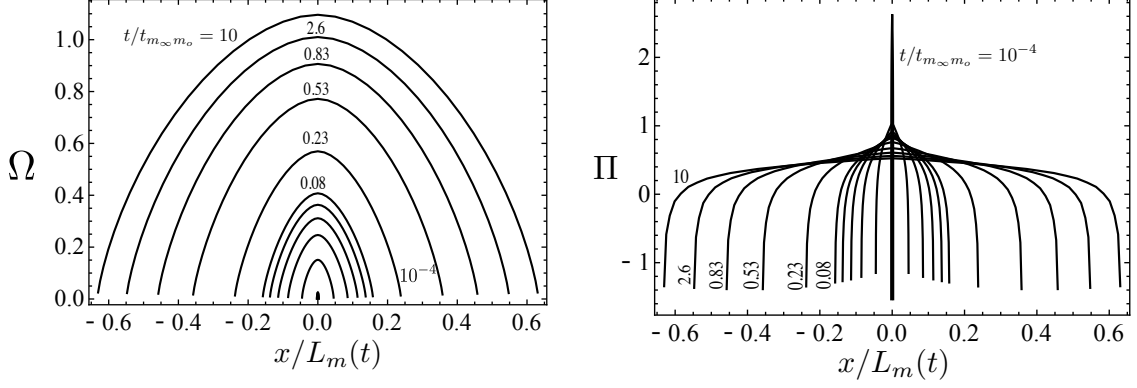
Figure 4: Profile of the dimensionless fracture opening (left) and net pressure (right) in a plane-strain hydraulic fracture driven by a Carreau fluid at different dimensionless times τ - $n = 0.5$, $\mu_\infty/\mu_0 = 0.01$ and $\mathcal{K} = 0.5$ case.

4.2.1 Initial solution

In order to start the simulation, an initial condition is required. As we have seen from the rheology of the Carreau fluid, at early dimensionless time, all the fluid in the fracture is at the viscosity $\mu = \mu_\infty$ (large shear rate cases). We thus use as initial condition the self-similar plane-stain hydraulic fracture solution for the corresponding dimensionless toughness $\mathcal{K}_\infty = \mathcal{K} \times (\mu_o/\mu_\infty)^{1/4}$. We actually also use a Gauss-Chebyshev quadrature scheme (as described in [17]) to obtain such a self-similar solution for any value of $\mathcal{K}_\infty$. We denote such an initial / early-time Newtonian solution with the μ_∞ viscosity as m_∞ in what follows- this for any value of the dimensionless toughness $\mathcal{K}_\infty$ which may be large and as such the growth may be toughness dominated early-on. Note, that we have to carefully convert this initial solution obtain with the μ_∞ viscosity scaling to the μ_o viscosity scaling used in our time evolution algorithm. As the initial solution is self-similar, we start from a small (but non-zero) time τ_{ini} taken to be sufficiently small such that the HF solution with μ_∞ is indeed valid. We typically use $\tau_{ini} = 10^{-5}$ in the results reported in the following section.

5 Results

5.1 Overall behaviour of the solution

Before varying the different dimensionless parameters such as the fluid index and viscosities ratio, it is worthwhile to first analyse the solution for a given set of dimensionless parameters. We use as a base case $n = 0.5$, $\mu_\infty/\mu_o = 0.01$ and a dimensionless toughness $\mathcal{K} = 0.5$. As such, at early time, the growth is between the viscosity and toughness dominated regimes as $\mathcal{K}_\infty = \mathcal{K} \times (\mu_\infty/\mu_o)^{-1/4} = 1.58$. We run a simulation for a dimensionless time ranging from $\tau = 10^{-5}$ to $\tau = 10$ in order to observe the transition from the early time m_∞ Newtonian solution to the large time m_o Newtonian solution.

The fracture width and net pressure profiles at different times are displayed on Fig. 4, while the time-evolution of fracture length, inlet pressure and width can be found on Fig. 5.

One can notably observe on Fig.4 that the net pressure gradient near the tip remains important while it decays with time in the central part of the fracture. This hints that the near tip region will be the last one one where the viscosity will tend towards μ_o.

The overall transition of the fracture growth is clearly visible from the time evolution of length, inlet width and inlet net pressure. At early time (for $\tau < 10^{-3} - 10^{-4}$), the fracture growth follows the Newtonian M_∞ solution, and tends exactly to the Newtonian M_o solution (for the given value of dimensionless toughness $\mathcal{K}$) at large time ($\tau > 1$). The fact that the growth

falls well on the M_o solution at large confirm that the choice of the characteristic time-scale $t_{m_\infty m_o}$ defined as the time at which the fluid characteristic shear stress falls in the low shear rate Newtonian plateau. It also validate the numerical method used.

The transition from the early to late time behavior is clearly visible with a change of slope around $\tau = 10^{-3}$ when the solution departs from the one where growth is governed by the large shear rate viscosity. Another change of slope occurs around $\tau \approx 1$, when the growth becomes controlled by μ_o. Interestingly, these change of slopes are more visible on the evolution of the inlet net pressure and to a lesser extent inlet width compared to the fracture length.

In figure 5, we have also displayed during the transition period, the corresponding solution for a power-law fluid rheology (denoted as the M_n solution). To perform such a comparison, we use the equivalence between the power-law consistency and Carreau rheological parameters using the same fluid index (see details in appendix). In the power-law case, a different time-scale emerges (see [2, 3]) and the solution becomes self-similar for a propagation time of the order of ten times the characteristic timescale of the power law problem. In that particular case, the power-law time-scale is about 10^4 times smaller than $t_{m_\infty m_o}$ such that for this given value of dimensionless toughness ($\mathcal{K} = 0.5$), the power-law growth is viscosity dominated and self-similar [2] (we denote it as M_n on figure 5).

One can see that the slopes of the Carreau and power law solutions are similar at the beginning of the transition (for $10^{-3} < \tau < 10^{-2}$). There is however a clear offset between the power law solution and the one obtained using the Carreau model. It is thus worth noting that even during the transition where the shear-thinning of the Carreau fluid is akin to a power-law (see Fig. 1), the growth obtained with a power-law rheology is significantly off from the solution for a Carreau rheology.

The evolution of the solution in between the large and low shear rates Newtonian plateaus can be physically grasped by looking at the profile of the tangent dimensionless viscosity Γ inside the fracture at different times as presented in Fig. 6. The spatial profile of $\Gamma(x/\ell)$ evolves between the large shear rate (early time) M_∞ limit (red line) and the low shear rate M_o limit at large time (blue line on Fig. 6). For intermediate time, the dimensionless viscosity profile has a characteristic inverted U-shape, with a strong gradient developing near the tip as time progresses. The tangent viscosity in the centre of the crack reaches unity (low shear rate plateau) for a dimensionless time close to $t/t_{m_\infty m_o} = 1$. A strong gradient develops near the tip as time progresses, but eventually disappear. Such an evolution is in line with the tip solution for a steadily moving fracture (with zero lag) as discussed in [13]: indeed three regimes where low and high shear Newtonian regions as well as a power-law regions can be present depending on the relative value of the viscosity ratio, fluid index and a dimensionless ratio of shear-stress (which in the tip scaling decreases with velocity). Figure 13 of [13] clearly illustrates that for low $\bar{\alpha}$ (which corresponds to small tip velocities therefore large time for a finite fracture under constant injection) the viscous asymptote corresponding to the high shear rate Newtonian plateau (μ_∞) ultimately disappears as well as the intermediate power-law region. This is clearly what happens here. We see from Fig. 6 that the fluid is completely at its low shear rate value for $\tau \approx 10$. For larger time, the details of the fluid rheology does not matter: the shear rate inside the fracture is low enough such that the fluid can be considered as Newtonian with a viscosity μ_o.

5.2 Influence of the dimensionless toughness $\mathcal{K}$

We now study the influence of the dimensionless toughness $\mathcal{K}$ on the solution, performing simulations for $\mathcal{K} = 0.5, 1.5, 3$, for the same viscosity ratio $\mu_\infty/\mu_o = 0.01$ and fluid index ($n = 0.5$). As such, the corresponding early time toughness (governed by μ_∞) are respectively 1.58, 4.74 and 9.48 (as $\mathcal{K}_\infty = \mathcal{K} \times (\mu_\infty/\mu_o)^{-1/4}$). The time evolution of the dimensionless fracture length for these three cases are reported on Fig. 7. As expected, the solutions evolves at late time to the M_o solutions corresponding to the different toughness values $\mathcal{K}$ (we do not display here all these solutions on Fig. 7 to avoid crowding the plot). For $\mathcal{K} = 3$, the solution is nearly toughness
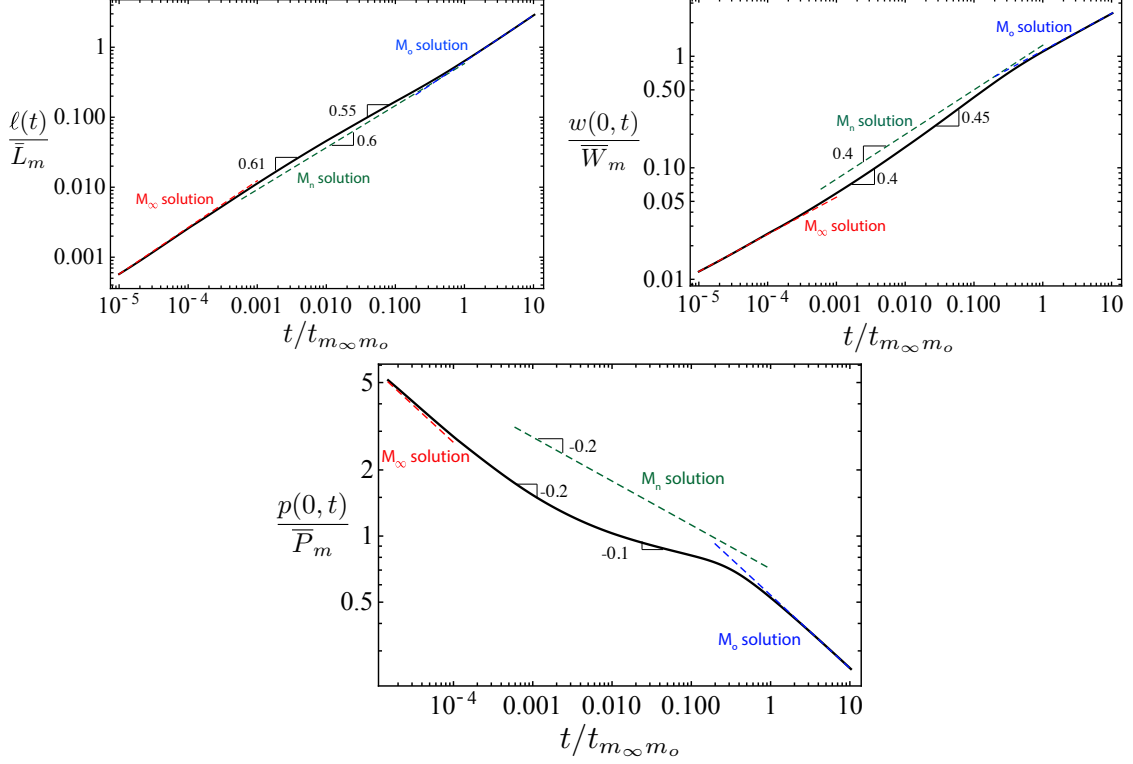
Figure 5: Dimensionless physical quantities as a function of a dimensionless time $t/t_{m_\infty m_o}$ in log-log scale - $n = 0.5$, $\mu_\infty/\mu_0 = 0.01$ and $\mathcal{K} = 0.5$ case. We also plot the corresponding infinite viscosity Newtonian solution (M_∞, solution in dashed red), μ_o viscosity Newtonian solution (M_o solution in dashed blue) and the viscosity dominated power law solution (M_n solution in dashed green). (a) dimensionless central opening $w(0,t)/\overline{W}_m$ where $\overline{W}_m = \varepsilon_m(t_{m_\infty m_o})L_m(t_{m_\infty m_o})$ (b) dimensionless length of the fracture $\ell(t)/\overline{L}_m$ (c) dimensionless central pressure $P(0,t)/\overline{P}_m$ where $\overline{P}_m = \varepsilon_m(t_{m_\infty m_o})E'$.
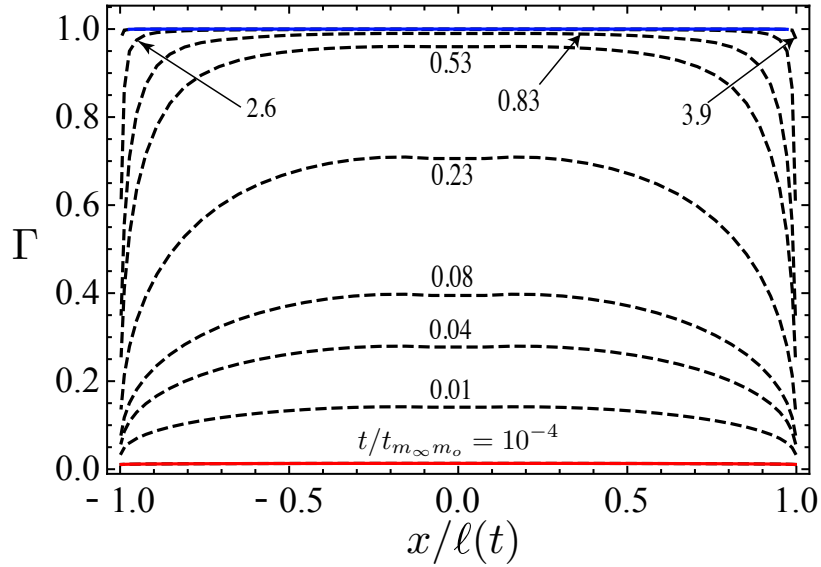

Figure 6: Dimensionless tangent viscosity profile Γ as a function of the dimensionless coordinate $\xi = x/\ell(t)$ for different dimensionless time : $\tau =$ (0.0001 (red line), 0.01, 0.04, 0.08, 0.23, 0.53, 0.83, 2.6, 3.9, 10.(blue line)). The parameters for this simulation are $n = 0.5$, $\mu_\infty/\mu_o = 0.01$ and $\mathcal{K} = 0.5$.
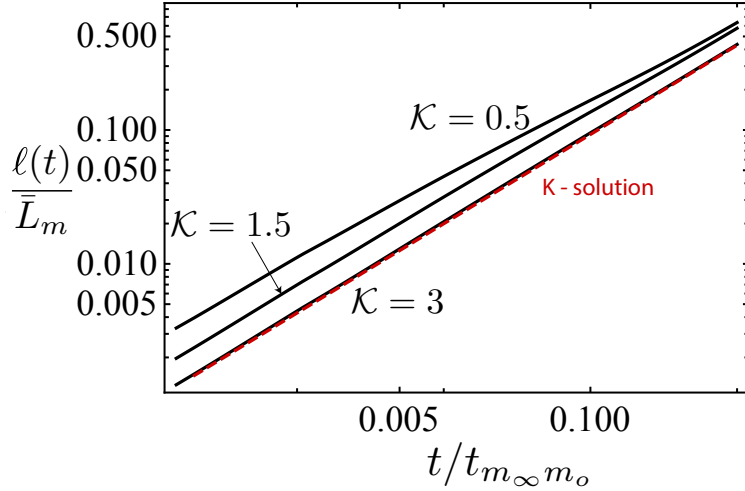
Figure 7: Evolution of the dimensionless length of the fracture in function of the dimensionless time for four different $\mathcal{K} = 0.5, 1.5, 3$, a fluid index $n = 0.5$ and a viscosity ratio $\mu_\infty/\mu_o = 0.01$ (black curves) and Newtonian toughness dominated solution for $\mathcal{K} = 3$ (dashed red curve).

dominated at all times: it follows perfectly the toughness dominated solution (reported in red dashed line as the K-solution). This is to be expected as $\mathcal{K}_\infty = 9.48$ for $\mathcal{K} = 3$, and as discussed in [27], the difference with the fully toughness dominated solution is within 5 percent for $\mathcal{K} > 3.7$.

This confirms the triangular propagation diagram of Fig. 3, which depicts the fact that if the late time / low shear rate dimensionless toughness $\mathcal{K} \gtrsim 3.7$ the growth is fully toughness dominated at large time, it is also toughness dominated at early time. In other words, the details of the fluid rheology do not matter. Interestingly, for lower values of $\mathcal{K}$ for which the growth is viscosity dominated ($\mathcal{K} \lesssim 1.3$) or intermediate ($1.3 \lesssim \mathcal{K} \lesssim 3.7$) at large time, the growth can initially be toughness dominated due to the relation $\mathcal{K}_\infty = \mathcal{K} \times (\mu_\infty/\mu_o)^{-1/4}$. This is notably the case here for $\mathcal{K} = 0.5$ ($\mathcal{K}_\infty = 1.58$) .

5.3 Influence of the viscosity ratio

We now investigate the influence of the rheological parameters of the Carreau model on the behaviour of the solution, starting with the viscosity ratio. For this, we focus on the evolution of the central opening and the length of the crack which are displayed in Fig. 8. It can be observed on the dimensionless viscosity in function of the shear stress at the wall (Fig. 2) that the viscosity ratio impacts only the value of the dimensionless tangent viscosity for large enough wall shear stresses. The rheology is insentive to the viscosity ratio for low shear stress (Fig. 2).

The influence of the ratio is thus especially decisive at early time, because it determines the asymptote that the solution initially follows as $\mathcal{K}_\infty = \mathcal{K} \times (\mu_\infty/\mu_o)^{-1/4}$. At large times, the solutions converge towards the Newtonian (M_o) solution for the corresponding value of $\mathcal{K}$ (0.5 here). On the curves of Fig. 8, we can observe that although the solutions for different viscosity ratios are initially apart at early times, they eventually merge during the transition period even before converging to the Newtonian solution μ_o (especially for the two smaller ratios). This is because the shear stress values falls within the range where the corresponding tangent viscosity values are very close for all three cases. In order to fully appreciate this phenomenon, it is interesting to study the evolution of the viscosity profile within the fracture as displayed on Fig. 9. At the beginning of the propagation, these viscosities profile are very different, but as time progresses, the profiles from the smaller to the larger viscosity ratio collapse and eventually reaches the full Newtonian low shear rate limit ($\Gamma = 1$ everywhere). It can be seen on Fig. 9 that the $\mu_\infty/\mu_o = 0.001$ case first catch up with the curve for $\mu_\infty/\mu_o = 0.01$. Keeping in mind
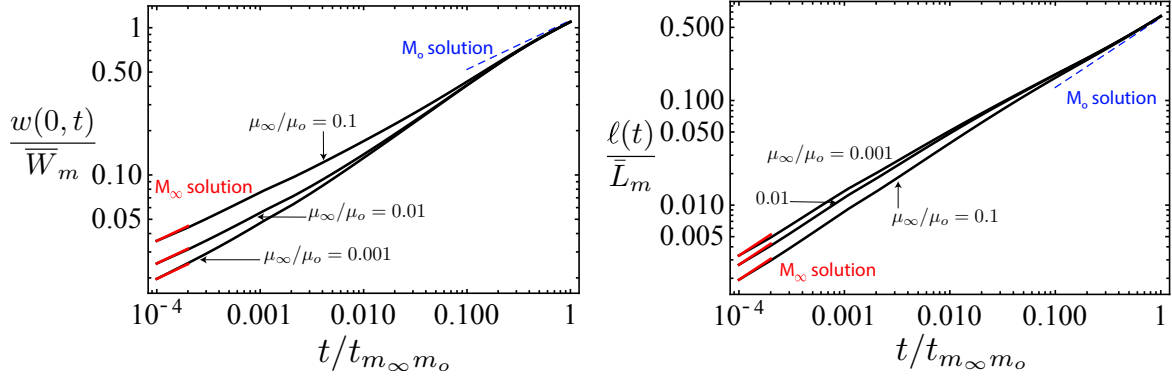
13

Figure 8: Evolution of the physical quantities as a function of the dimensionless time t/t_m in loglog scale for $\mathcal{K} = 0.5$, $n = 0.4$ and three different values of the viscosity ratio $\mu_\infty/\mu_o = 0.1, 0.01, 0.001$. We also plot the viscosity dominated Newtonian solutions computed with the infinite viscosity (M_∞ red curve) and the μ_0 viscosity (M_o dashed blue curve). (a) dimensionless central opening of the fracture $w(0,t)/\overline{W}_m$ where $\overline{W}_m = \varepsilon_m(t_{m_\infty m_o})L_m(t_{m_\infty m_o})$ (b) dimensionless length of the fracture $\ell(t)/\overline{L}_m$.

the viscosity - shear stresses profiles of Fig. 2, we can observe the phase where these two curves are equal ($\tau_w < 0.1$). It is also understandable why the $\mu_\infty/\mu_o = 0.1$ profile is caught up just before the M_o solution. Again, we can refer to the rheological profiles (Fig. 2-viscosity ratio panel), where we observe that the two curves (for 0.1 and 0.01) merges only shortly before the low shear-rate Newtonian plateau. This tendency intrinsic to the rheology and Poiseuille type flow is thus found in the HF propagating solution.

5.4 Influence of the power law index n

The power-law index n controls how steep the fluid transition between the low and high shear rates viscosity limits. The greater the n, the larger is the shear-thinning region (see e.g.**??**-n panel) while the limit of the low shear rate plateau is unchanged. As a result, for larger n, the longer will be the transition of the propagation solution between the early and late time Newtonian regimes. However, we have seen that the characteristic time of the problem does not depend on n (i.e. the limit of the low shear rate plateau do no depend on n). We therefore expect the transition phase to end approximately at the same time regardless of the value of n. The transition is expected to start at distinct times, with shorter transition in the case of smaller values of n. We performed simulations for four n values $(0.2, 0.4, 0.6, 0.8)$ spanning realistic values of the fluid index. The time evolution of length and inlet width are reported on Fig. 10, while the viscosity profiles at different times are displayed on Fig. 11.

We indeed observe the strong effect of n on the departure from the early time / large viscosity solution. For $n = 0.8$, we observe for example that even for very early time, the solution is already in the transition phase. The transition period starts later and is significantly shorter for smaller n (0.4 and 0.2)). All solutions for the different power-law indices merge at about $t/t_{m_\infty m_o} = 1$, which is consistent with the rheological behaviour as this time scales is defined by the critical shear rate at which the fluid starts to shear-thin. The convergence of all the viscosity profiles in time can be clearly observed from the four snapshots reported on Fig. 11, with the profiles for the different values of n already very similar throughout the fracture at $t/t_{m_\infty m_o} = 0.8$.

6 Discussions

It is interesting to compare the results obtained for HF growth on a specific case when using either the Carreau or the power-law model. To do so, we use the rheological parameters for a
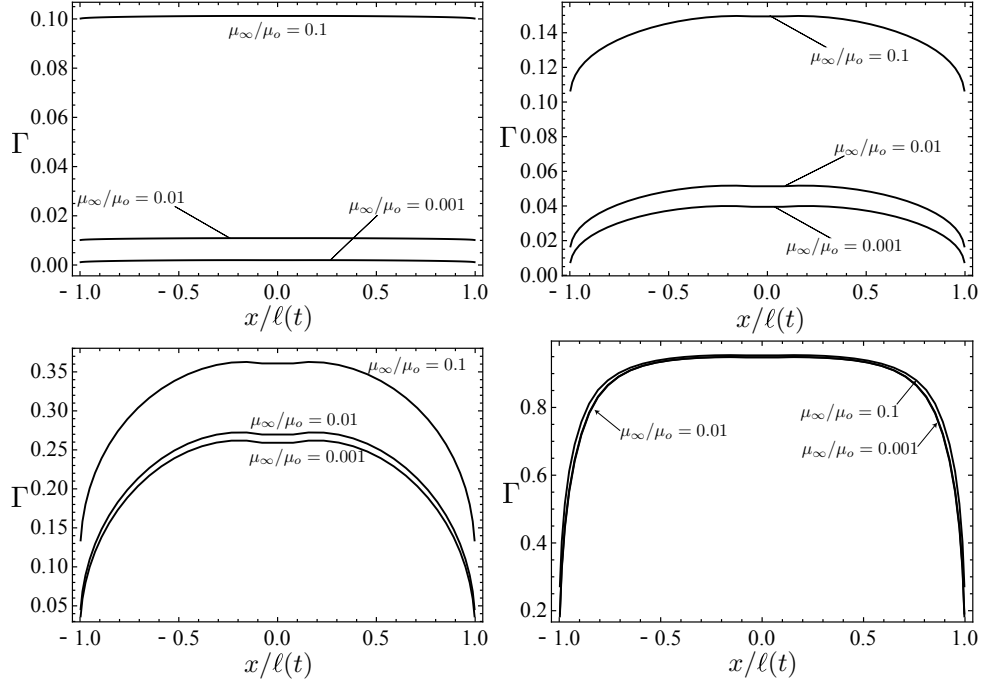
Figure 9: Dimensionless viscosity profile as a function of the dimensionless coordinate $\xi = x/\ell(t)$ at four different dimensionless time $t/t_{m_\infty m_o}$=(0.0001, 0.0101, 0.0692, 0.4803) for $n = 0.4$ and for three different values of the viscosity ratio $\mu_\infty/\mu_o = 0.1, 0.01, 0.001$ and $\mathcal{K} = 0.5$.
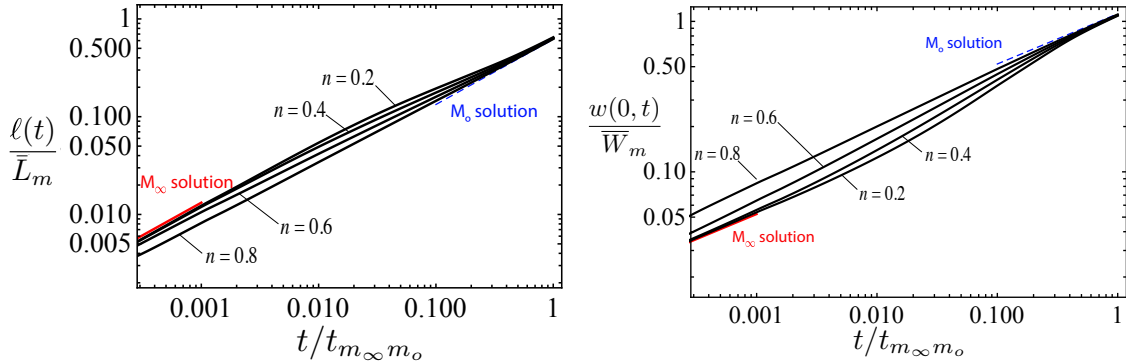

Figure 10: Evolution of the physical quantities as a function of the dimensionless time $t/t_{m_\infty m_o}$ in loglog scale for a viscosity ratio of $\mu_\infty/\mu_o = 0.01$ and dimensionless toughness $\mathcal{K} = 0.5$ and four different values of the power number $n = 0.2, 0.4, 0.6, 0.8$. We also plot the viscosity dominated Newtonian solutions computed with the infinite viscosity μ_∞ (M_∞ red curve) and the μ_o viscosity (M_o dashed blue curve). (a) dimensionless length of the fracture $l(t)/L_m(t)$ (b) dimensionless central opening of the fracture $w(0,t)/\overline{W}_m$ with $/\overline{W}_m = \varepsilon_m(t_{m_\infty m_o})L_m(t_{m_\infty m_o})$.
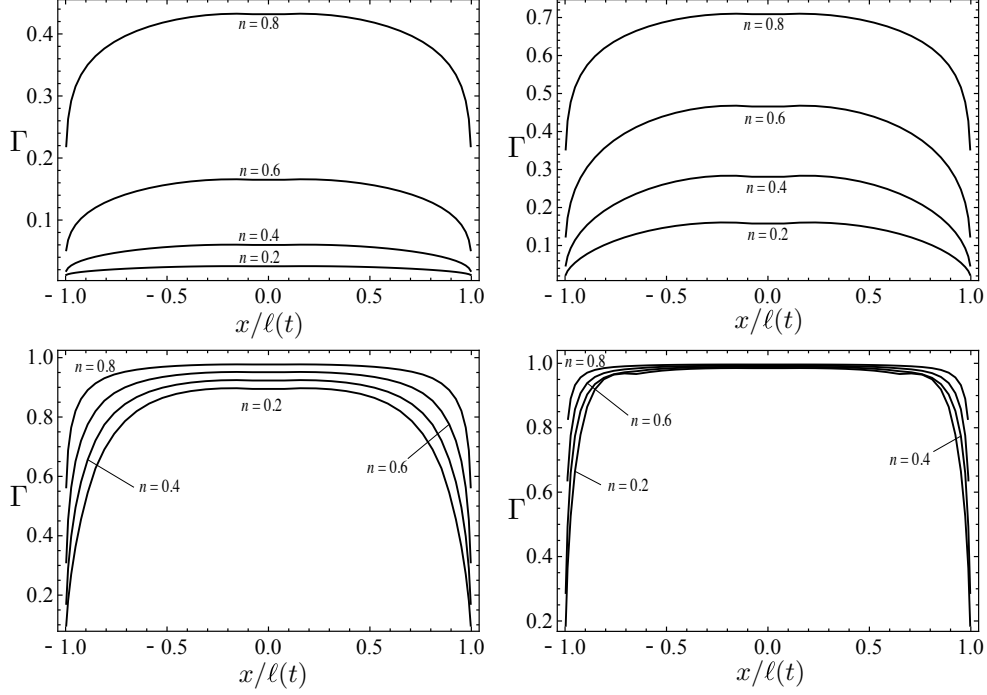
15

Figure 11: Dimensionless viscosity profile as a function of the dimensionless coordinate $\xi = x/\ell(t)$ at four different dimensionless time $t/t_{m_\infty m_o} = (0.012, 0.07, 0.4, 0.8)$ for four different values of the fluid index $n = 0.2, 0.4, 0.6, 0.8$ - $\mu_\infty/\mu_0 = 0.01$ and $\mathcal{K} = 0.5$.

HPG fluid as reported below (see [29] and also [13]):

	n	μ_o (Pa.s)	μ_∞ (Pa.s)	$\dot{\gamma}_c$ (s^{-1})
HPG (15°C)	0.46	0.44	0.001	3.3

The corresponding value of the consistency index of the power-law model is $M = 0.75$ Pa.s^n. We assume $E' = 30 GPa$ and $K' = 1.5$ MPa.$\sqrt{m}$ for the rock properties and an injection rate $Q_o = 4.10^{-4} m^2/s$. For these parameters, the dimensionless toughness is $\mathcal{K} = 0.1$, and $\mu_\infty/\mu_o = 0.002$.

The evolution of fracture length, inlet width and inlet net pressures is reported in Fig. 12 for an injection lasting of one hour.

In case of the power-law model, a physically different characteristic time t_{PL} emerges (see [2, 3] and appendix B) which corresponds to the time at which the viscosity dominated solution becomes valid. On the other hand for the Carreau model, the characteristic time (t_m) corresponds to the time when the solution converges towards the zero shear rate Newtonian solution. For the values used here, these time scales are respectively $t_{PL} = 2.95$ seconds and $t_{m_\infty m_o} = 522691$ seconds (about 150 hours). We thus see that over the hour of propagation investigated here, the growth for the power-law model follows the viscosity dominated power-law solution derived in [2]. On the other hand, the Carreau solution has not yet completely finished converging towards the Newtonian solution after an hour of injection ($3600 < t_{m_\infty m_o}$). After an hour of injection the relative difference between the simpler power-law model compared to the Carreau one are respectively of 26.78%,-40.85% and -101% on fracture length, inlet width and net pressure respectively. In other words, the power-law model strongly under-estimates net pressure and fracture width while over-estimating fracture half-length.

These differences are significant, however, they are dependent on the characteristic time of the problem. Indeed, let's compare the results for a hypothetical fluid with the same rheological parameters except for the critical shear rate $\dot{\gamma}_c$ now taken as $\dot{\gamma}_c = 20$ (1/seconds). Using also lower value for the plane-strain Young's modulus $E' = 10$ GPa, we obtain after an hour of injection a

16

difference of the power-law compared to the Carreau model of 8.13%, -13.63% and -30.73% for length, inlet width and net pressure respectively. In this case, the Carreau characteristic time is about 3 hours (20 226 seconds), while t_{PL} remains low ($t_{PL} = 207.89$ seconds such that the power-law growth is strictly viscosity dominated). As a result, after one hour of injection, the Carreau solution is equal to the Newtonian solution at viscosity μ_o. As can be seen in Fig. 13, the difference between the solutions evolves with the dimensionless time, following the shear-thinning of the fluid which is best captured by the Carreau model. The power-law estimates are always under predicting the fracture length, over predicting the net pressure and width.

7 Conclusions

In view of the extensive use of shear-thinning fluids in hydraulic fracturing practice, it is important to take the appropriate shear thinning behaviour into account. For a plane-strain geometry and a Carreau fluid, we have shown that the propagation at early-time is following the Newtonian one with the large shear-rate viscosity, then departs from it and evolves at late time to the low shear-rate Newtonian solution.

The characteristic time-scale of transition $t_{m_\infty m_o} = 12^{3/2} E'^{1/2}/(\mu_o'^{1/2} \dot{\gamma}_c^{3/2})$ controls the time where the solution converges toward the low-shear rate Newtonian plateau: it does not depend neither on n nor the viscosity ratio. One has to note that $t_{m_\infty m_o}$ can vary significantly depending on the fluid and rock properties spanning a very large range (from 200 up to 10^8 seconds) for realistic values. This time-scale $t_{m_\infty m_o}$ allows to easily grasp the importance of shear-thinning for a particular case in comparison to the injection duration. If $t_{m_\infty m_o}$ is small compared to the injection duration, the fluid will always have a Newtonian behaviour (with the low shear rate viscosity) during most of the operation - the use of a Newtonian rheology with a viscosity equals to μ_o is warranted. Similarly, if $t_{m_\infty m_o}$ is large compared to the injection duration, the use of a Newtonian rheology with μ_∞ properly captures the HF evolution. It is interesting to note that the effort of making a polymer fluid (to obtain larger width) in hydraulic fracturing can be lost if $t_{m_\infty m_o}$ is much larger than the injection duration as in that particular cases, the solvent viscosity μ_∞ controls the hydraulic fracture evolution during most of the injection. Decreasing $t_{m_\infty m_o}$ via notably large value of the critical shear-rate $\dot{\gamma}_c$ is a key engineering target.

If the injection duration is comparable to $t_{m_\infty m_o}$, a large transition period occurs (see for example the case of the HPG fluid discussed previously where the solution is still in the transition phase after one hour of injection). The departure from the early-time / large-shear rate Newtonian solution occur faster for value of the fluid index closer to 1. The viscosity ratio also plays a crucial role in the intensity of the overall shear-thinning effect. It is also worth re-emphasizing that the solution at early time is controlled by a dimensionless toughness ($\mathcal{K}_\infty = \mathcal{K} \times (\mu_\infty/\mu_o)^{-1/4}$) which may be significantly larger than the late time dimensionless toughness $\mathcal{K}$ for small viscosity ratio (μ_∞/μ_o). In other words, the propagation can be dominated by toughness at early time and viscosity at late times.

Figure 13 displays another example for the fracture length evolution (viscosity dominated at late time, transitional at early time). Again, one can see that the Carreau solution "follows" the structure of the rheology. When the shear rate begins to decrease, the solution begins its transition to the Newtonian solution μ_o, the fracture behaves for a short intermediate period of time like the one driven by a power law fluid (with the same slope in time but with an offset). However, it finally ends up following the μ_o Newtonian solution for times larger than $t_{m_\infty m_o}$.

Another important conclusion is that using a power-law rheology never gives realistic results compared to the Carreau model. The power-law model should be simply abandoned in hydraulic fracture modeling. This is intrinsically due to the fact that the power-law model yields unrealistically small tangent viscosity at high shear rates, respectively unrealistically large tangent viscosity at low shear rates. The range of shear rate occurring in hydraulic fracturing is so wide that capturing only the shear-thinning part of the rheology is not a proper strategy. Missing the
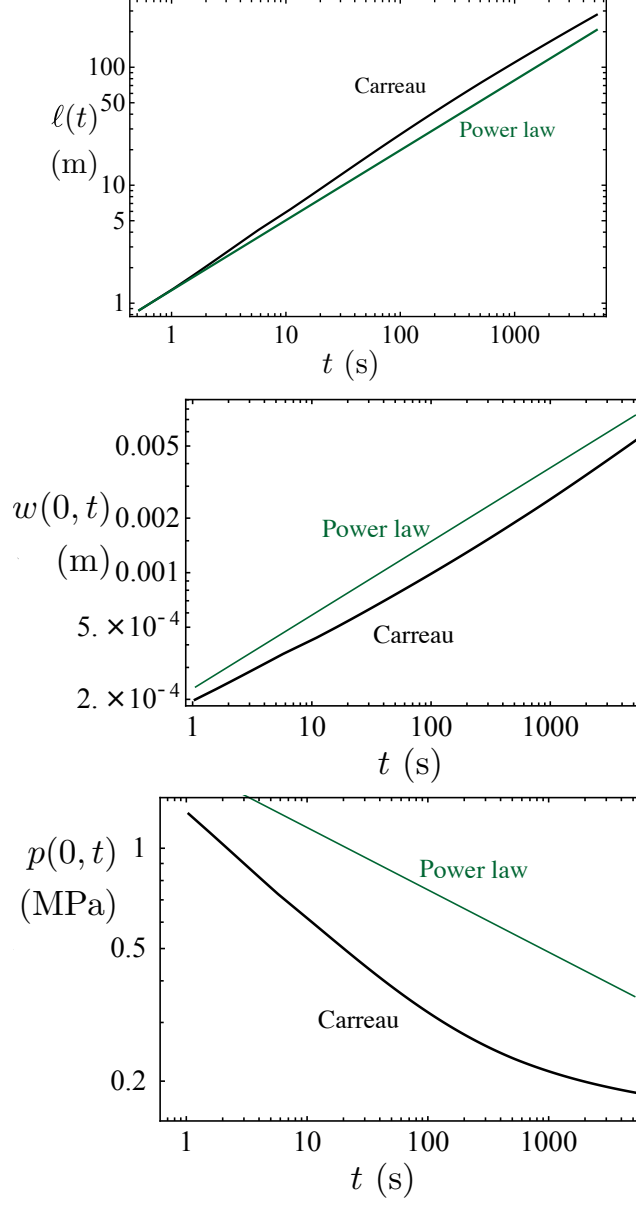
Figure 12: Results of a dimensional simulation for a HPG fluid using either a Power law or a Carreau rheological model, (a) length (m) of the fracture as a function of the time (s) in log-log scale (b) central opening (m) as the function of the time (s) in log-log scale (c) central pressure (Pa) as the function of the time (s) in log-log scale. For the power law model, the viscosity dominated solution obtained in [2] is displayed.
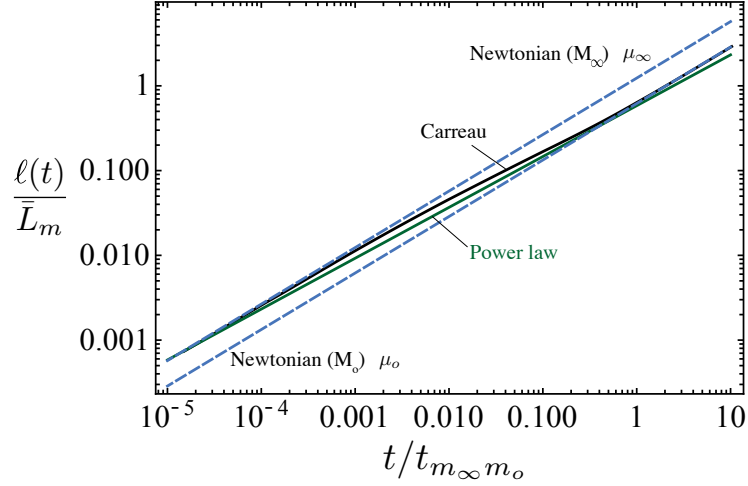
Figure 13: Evolution of the dimensionless length of the fracture using theCarreau, Power law and the Newtonian (for $\mu = \mu_o$ and $\mu = \mu_\infty$) models as a function of dimensionless time for $n = 0.46$, $\mu_\infty/\mu_o = 0.002$ and $\mathcal{K} = 0.3$ ($\mathcal{K}_\infty = 1.5$) .

large or low shear rate plateau (as the power-law model does) results in a significant error.

The scaling and structure of the solution provided here for a plane-strain fracture allow to easily quantify the importance of shear-thinning on hydraulic fracture growth for a particular set of rock, fluid properties and injection conditions. The case of a radial fracture geometry will exhibit similar features with in addition a competition between the evolution of the dimensionless toughness (which in the radial case depends on time) and the fluid shear-thinning behavior.

Credit author statement

- Lucas Pereira: Conceptualization, Investigation, Methodology, Software, Visualization, Writing - original draft.

- Brice Lecampion: Conceptualization, Investigation, Methodology, Visualization, Supervision, Writing - review and editing.

Data Availability Statement Data sharing not applicable – no new data generated.

A   Parallel plate flow of a Carreau fluid

For completeness, we here briefly recall the expression derived in [12] for the flow of a Carreau fluid in pressure-driven parallel plate flow. The dimensionless apparent viscosity $\Gamma\left(\tau_w, \dot{\gamma}_c, n, \mu_\infty/\mu_o\right)$ appearing in Eq. (6) can be expressed from the shear stress at the wall τ_w as

$$\Gamma\left(\tau_w/(\mu_o\dot{\gamma}_c), \mu_\infty/\mu_o, n\right) = \frac{\left(\tau_w/(\mu_o\dot{\gamma}_c)\right)^3}{3I(\dot{\gamma}_w/\dot{\gamma}_c, \mu_\infty/\mu_o, n)} \tag{32}$$

where $I(\dot{\gamma}_w/\dot{\gamma}_c, \mu_\infty/\mu_o, n)$ is an analytical function of the the wall shear rate $\dot{\gamma}_w$ derived in [12]:

$$I(\dot{\gamma}_w, \dot{\gamma}_c, \mu_\infty/\mu_o, n') = n'\delta^2\left(\dot{\gamma}_w/\dot{\gamma}_c\right)\left[{}_2F_1\left(\frac{1}{2}, 1-n'; \frac{3}{2}; -\left(\dot{\gamma}_w/\dot{\gamma}_c\right)^2\right) - {}_2F_1\left(\frac{1}{2}, -n'; \frac{3}{2}; -\left(\dot{\gamma}_w/\dot{\gamma}_c\right)^2\right)\right] +$$

$$n'\delta(1-\delta)(\dot{\gamma}_w/\dot{\gamma}_c)\left[{}_2F_1\left(\frac{1}{2}, 1-\frac{n'}{2}; \frac{3}{2}; -\left(\dot{\gamma}_w/\dot{\gamma}_c\right)^2\right) - {}_2F_1\left(\frac{1}{2}, -\frac{n'}{2}; \frac{3}{2}; -\left(\dot{\gamma}_w/\dot{\gamma}_c\right)^2\right)\right] + \frac{(1-\delta)^2(\dot{\gamma}_w/\dot{\gamma}_c)^3}{3}$$

$$+\frac{(1+n')\delta^2(\dot{\gamma}_w/\dot{\gamma}_c)^3\,{}_2F_1\left(\frac{3}{2}, -n'; \frac{5}{2}; -\left(\dot{\gamma}_w/\dot{\gamma}_c\right)^2\right)}{3} + \frac{(2+n')(1-\delta)\delta(\dot{\gamma}_w/\dot{\gamma}_c)^3\,{}_2F_1\left(\frac{3}{2}, -\frac{n'}{2}; \frac{5}{2}; -\left(\dot{\gamma}_w/\dot{\gamma}_c\right)^2\right)}{3}$$

with $n' = n-1$, $\delta = 1-\mu_\infty/\mu_o$, and ${}_2F_1$ is the hypergeometric function with real variables. The shear rate at the wall $\dot{\gamma}_w$ is related to the wall shear stress τ_w via the Carreau rheological Eq. (5).

B   Power-law rheology

For comparisons purposes, we briefly recall here the scalings for the propagation of plane-strain hydraulic fracture driven by a power-law fluid. In the case of a power law fluid, the Poiseuille lubrication equation has the following analytical expression:

$$q|q|^{n-1} = -\frac{w^{2n+1}}{M'}\frac{\partial p}{\partial x} \tag{33}$$

with $M' = 2^{2n+1}\frac{(2n+1)^n}{n^n}M$ (M has dimension $Pa.s^n$). The power-law consistency M can be expressed directly from the rheological parameters of the Carreau model (see [13] for example):

$$M = \frac{\mu_0 + \mu_\infty}{2\dot{\gamma}_c^{n-1}(2^{-2/(n-1)} - 1)^{(n-1)/2}} \tag{34}$$

keeping the same power-index n. We can re-write the Poiseuille lubrication flow relation for a power-law fluid (33) in a similar way than for the Carreau rheology eq.(6). We obtain the following expression for the power-law dimensionless viscosity Γ_{PL} as function of the wall shear-stress $\tau_w = \frac{w}{2}\left|\frac{\partial p}{\partial x}\right|$:

$$\Gamma_{PL} = \frac{2^{(n-1)/n}M'^{1/n}\tau_w^{(n-1)/n}}{3\mu_o} \tag{35}$$

which can be expressed in function of the Carreau rheological parameters thanks to Eq. (34).

Following a scaling analysis similar to the one of the main text (see [2, 3] for more details), one obtains the following dimensionless numbers for plane-strain HF growth driven by a power-law rheology:

$$\mathcal{G}_v = \frac{Q_o t}{\varepsilon L^2} \qquad \mathcal{G}_m = \frac{M'Qo^n}{E'\varepsilon^2(\varepsilon L)^{2n}} \qquad \mathcal{G}_k = \frac{K'}{\varepsilon E'L^{1/2}} \tag{36}$$

Similarly than for the Newtonian case, two different scalings appear. We start by the K-scaling where both G_k and G_v are set to 1.

$$\epsilon_k = \left(\frac{K'^4}{E'^4 Q_0 t}\right)^{1/3} \qquad L_k = \left(\frac{E'Q_0 t}{K'}\right)^{2/3} \qquad \mathcal{M} = t^{2(1-n)/3}Q_0^{(2+n)/3}M'K'^{-4(n+2)/3}E'^{5/3+4n/3} \tag{37}$$

defining a characteristic time-scale

$$t_{PL} = \frac{K'^{2(2+n)/(1-n)}}{E'^{(5+4n)/(2(1-n))}M'^{3/(2(1-n))}Q_o^{(2+n)/2(1-n)}} \tag{38}$$

This characteristic time corresponds to the time needed for the dimensionless toughness to be equal to 1, so for larger times the solution will be in the viscosity dominated regime (since $\mathcal{K}$ is decreasing). The dimensionless viscosity can be expressed as $\mathcal{M} = (t/t_{PL})^{2(1-n)/3}$.

For the M-scaling (viscosity dominated), we have the following expressions:

$$\epsilon_m = E'^{-1/(2+n)}M'^{1/(2+n)}t^{-n/(2+n)} \tag{39}$$

$$L_m = E'^{1/(4+2n)}M'^{-1/(4+2n)}Q_o^{1/2}t^{(1+n)/(2+n)} \tag{40}$$

$$\mathcal{K}(t) = (t/t_{PL})^{(n-1)/(2(2+n))} \tag{41}$$

The complete solution evolving from the toughness dominated solution at early time to the viscosity dominated solution at large time can be found in [3]. The late time viscosity dominated solution (M_n self-similar solution) derived in [2] is valid for $t \gg t_{PL}$, i.e. for $\mathcal{M} > 10$ (see discussion in [3]).

C   Numerical algorithm

We describe a numerical method for the solution of the complete evolution problem from a given initial state. Our method is based on a non-uniform moving mesh discretized using a Gauss-Chebyshev quadrature and a collocation method. Extrapolation, integration, and differentiation operations are simplified as matrix multiplications using Barycentric techniques (see [16] for more details). We turn the fully coupled hydraulic fracture propagation problem into a system of non-linear ordinary differential equations (ODEs) in time that can then be integrated in time via a fully implicit scheme.

C.1   Gauss-Chebyshev quadrature

The method makes use of a primary $s = s_j$, $j = 1, ..., n$, and a complimentary $z = z_i$, $i = 1, ..., m$ sets of nodes, discretizing the fracture interval $[-1, 1]$, which corresponds to the roots of the respective Chebyshev polynomials $\phi_n(s)$ and $\Psi_m(z)$. Specifically, the square-root singularity of linear elastic fracture mechanics can be directly embedded in the discretization. The dislocation density is expressed as:

$$\frac{\mathrm{d}w}{\mathrm{d}s} = \omega(s)F(s), \quad \omega(s) = \frac{1}{\sqrt{1-s^2}} \tag{42}$$

where $\omega(s)$ is a weight function with the required tip singularity and $F(s)$ an unknown non-singular function. For the type of singularity embedded in Eqns (26)-(27), the primary and complimentary polynomials are the Chebyshev of the first $\phi_n(s) = T_n(s)$, and second $\Psi_m(z) = U_m(z)$ (with $m = n - 1$) kinds respectively [16]. The corresponding two sets of spatial nodes are given by:

$$s_j = \cos(\frac{\pi(j-1/2)}{n}), j = 1, ..., n \quad z_i = \cos\frac{\pi i}{n}, i = 1, ..., n-1 \tag{43}$$

C.2   Hilbert transform operator for the dislocation density

The plane-strain elastic equation reduces to the well-known Hilbert transform

$$\mathcal{H}[w](z) = \frac{1}{\pi}\int_{-1}^{1}\frac{1}{z-s}\frac{\partial w}{\partial s}\,\mathrm{d}s \tag{44}$$

which is evaluated on the complimentary z-set of nodes using representation of the dislocation density on the s-set, $F(s_j)$. This results in the following:

$$\mathcal{H}[w](z_i) = \sum_{j=1}^{n} \mathcal{H}_{ij} F(s_j), \quad \mathcal{H}_{ij} = \frac{1}{n} \frac{1}{z_i - s_j} \tag{45}$$

C.3 Operators for extrapolation and integration

The unknown function F representing the unknown dislocation density can be extrapolated from the Gauss-Chebyshev nodes to the fracture tip:

$$F(-1) = \sum_{j=1}^{n} P_j F(s_j), \quad F(1) = \sum_{j=1}^{n} Q_j F(s_j) \tag{46}$$

where :

$$P_j = (-1)^j \frac{\tan \arccos s_j / 2}{n}, \quad Q_j = -(-1)^j \frac{\cot \arccos s_j / 2}{n} \tag{47}$$

Integration operators can be defined on either grid with the result of integration on the same or the other grid. For example, consider integration of the dislocation density:

$$\int_{z_i}^{1} \frac{\partial w}{\partial s} \, ds = -\sum_{j=1}^{n} S_{ij} F(s_j), \quad S_{ij} = \sum_{k=0}^{n-1} [\phi_k(z_i) - \phi_k(1)] B_{kj} \tag{48}$$

where ϕ_k is the Chebyshev polynomial and

$$B_{kj} = \frac{2}{n} \cos \frac{\pi k (j - 1/2)}{n} \tag{49}$$

and $B_{0j} = 1/n$, we can define the following operators:

$$\int_{-1}^{1} \frac{\partial w}{\partial s} ds = \sum_{j=1}^{n} S_{Aj} F(s_j), \quad S_{Aj} = \sum_{k=0}^{n-1} [\phi_k(1) - \phi_k(-1)] B_{kj} \tag{50}$$

$$\int_{0}^{1} \frac{\partial w}{\partial s} ds = \sum_{j=1}^{n} S_{Hj} F(s_j), \quad S_{Hj} = \sum_{k=0}^{n-1} [\phi_k(1) - \phi_k(0)] B_{kj} \tag{51}$$

We also have:

$$\int_{z_i}^{1} \xi \frac{\partial w}{\partial \xi} d\xi = -\mathbf{S}.(\mathbf{sF}) \tag{52}$$

where $\mathbf{S}$ is a matrix S_{ij}, $\mathbf{F}$ a vector containing F_i and $\mathbf{s}$ contains the s-set coordinates. A derivative operator can be defined, for a regular $f(z)$ function:

$$f'(z_i) = \sum_{l=1}^{n} D_{il} f(z_i) \tag{53}$$

C.4 Discretized governing equations

The elasticity equations transforms into the following matrix equation as

$$\frac{1}{4\pi\gamma} \mathcal{H}_{ij}.F_j = \Pi_i \tag{54}$$

The lubrication flow equation becomes after integrating the equation between z_i and 1:

$$-\mathbf{z} \frac{\partial}{\partial \tau} (\mathbf{S}.\mathbf{F}) + \frac{\partial}{\partial \tau} (\mathbf{S}.(\mathbf{sF})) + \frac{1}{\gamma} \frac{d\gamma}{d\tau} (\mathbf{S}.(\mathbf{sF})) = \frac{(\mathbf{S}.\mathbf{F})^3}{\mathbf{\Gamma}(\tilde{\tau}_w, \mu_\infty/\mu_o, n)} \mathbf{D}.\mathbf{\Pi} \tag{55}$$

22

where $\tilde{\boldsymbol{\tau}}_w$ is the dimensionless wall shear stress at the z-points obtained as $\frac{1}{2\gamma}(\mathbf{S.F})(\mathbf{D.\Pi})$. The global continuity equation becomes (with $\mathbf{S_H} = S_{Hj}$):

$$2\gamma \mathbf{S_H}.(\mathbf{sF}) = \tau \tag{56}$$

while the propagation criterion becomes (where $\mathbf{Q} = Q_i$):

$$\mathbf{Q.F} = -\frac{\mathcal{K}\sqrt{\gamma}}{\sqrt{2}} \tag{57}$$

This allows to construct a system of non-linear ordinary differential equations solving for the unknowns F_i at the s-nodes and the dimensionless fracture length γ.

To solve the problem, we will use an implicit algorithm in order to get rid of the temporal derivative. Considering that we know the solution at a time τ_n, we will solve the following system to find the solution at τ_{n+1}, we discretize the lubrication equation, but we also derivate in time the three others equations. We replace the partial time derivative using a simple finite difference:

$$\frac{\partial \gamma}{\partial \tau} = \frac{\gamma_{\tau+\Delta\tau} - \gamma_\tau}{\Delta\tau} \tag{58}$$

$$\frac{\partial \Omega}{\partial \tau} = \frac{\Omega_{\tau+\Delta\tau} - \Omega_\tau}{\Delta\tau} \tag{59}$$

Knowing that α depends on time, we will have to generate a new $\Gamma(\mu_{inf}/\mu_0, n, \alpha, \tau_w)$ at each step of the computation. The final system to be solved therefore consists in

- the continuity equation collocated on the z-nodes

$$\frac{\Delta\tau}{\gamma^2_{\tau+\Delta\tau}\Gamma(F_{\tau+\Delta\tau}, \gamma_{\tau+\Delta\tau})}(\mathcal{S}.F_{\tau+\Delta\tau})^3\mathcal{D}.P + z(\mathcal{S}.(F_\tau - F_{\tau+\Delta\tau}) - (2 - \frac{\gamma_\tau}{\gamma_{\tau+\Delta\tau}}\mathcal{S}.(sF_{\tau+\Delta\tau}) + \mathcal{S}.(sF_\tau) = 0 \tag{60}$$

- the propagation condition:

$$-\mathcal{Q}(F_{\tau+\Delta\tau} - F_\tau) = \mathcal{K}\frac{\gamma_{\tau+\Delta\tau} - \gamma_\tau}{2\sqrt{2\gamma_{\tau+\Delta\tau}}} \tag{61}$$

- and the global volume balance:

$$(\gamma_{\tau+\Delta\tau} - \gamma_\tau)\mathcal{S}_A(sF_{\tau+\Delta\tau}) + \gamma_{\tau+\Delta\tau}(\mathcal{S}_A(sF_{\tau+\Delta\tau}) - \mathcal{S}_A(sF_\tau)) + \Delta\tau = 0 \tag{62}$$

This system is strongly non linear due to the presence of F in the dimensionless viscosity. In order to obtain a solution at each time step, we use a Newton-Raphson scheme. The initial condition is taken as the Newtonian solution with the large shear-rate viscosity μ_∞.

References

[1] Barbati AC, Desroches J, Robisson A, McKinley GH. Complex Fluids and Hydraulic Fracturing. *Annual Review of Chemical and Biomolecular Engineering* 2016; 7: 415–453.

[2] Adachi JI, Detournay E. Self-similar solution of a plane-strain fracture driven by a power-law fluid. *International Journal for Numerical and Analytical Methods in Geomechanics* 2002; 26(6): 579–604. http://dx.doi.org/10.1002/nag.213 doi: 10.1002/nag.213

[3] Garagash DI. Transient solution for a plane-strain fracture driven by a shear-thinning, power-law fluid. *International Journal for Numerical and Analytical Methods in Geomechanics* 2006; 30(14): 1439–1475. http://dx.doi.org/10.1002/nag.535 doi: 10.1002/nag.535

[4] Detournay E. Propagation Regimes of Fluid-Driven Fractures in Imper-meable Rocks. *International Journal of Geomechanics* 2004; 4(1): 35–45. http://dx.doi.org/10.1061/(ASCE)1532-3641(2004)4:1(35) doi: 10.1061/(ASCE)1532-3641(2004)4:1(35)

[5] Detournay E. Mechanics of Hydraulic Fractures. *Annual Review of Fluid Mechanics* 2016; 48: 311–339.

[6] Lecampion B, Bunger AP, Zhang X. Numerical methods for hydraulic fracture propagation: A review of recent trends. *Journal of Natural Gas Science and Engineering* 2018; 49: 66-83. http://dx.doi.org/10.1016/j.jngse.2017.10.012 doi: 10.1016/j.jngse.2017.10.012

[7] Desroches J, Detournay E, Lenoach B, et al. The crack tip region in hydraulic fracturing. *Proceedings of the Royal Society of London. Series A: Mathematical and Physical Sciences* 1994; 447(1929): 39–48.

[8] Dontsov EV, Kresse O. A semi-infinite hydraulic fracture with leak-off driven by a power-law fluid. *Journal of Fluid Mechanics* 2018; 837: 210–229. http://dx.doi.org/10.1017/jfm.2017.856 doi: 10.1017/jfm.2017.856

[9] Adachi JI, Siebrits E, Peirce AP, Desroches J. Computer simulation of hydraulic frac-tures. *International Journal of Rock Mechanics and Mining Sciences* 2007; 44(5): 739–757. http://dx.doi.org/10.1016/j.ijrmms.2006.11.006 doi: 10.1016/j.ijrmms.2006.11.006

[10] Carreau PJ. Rheological equations from molecular network theories. *Transactions of the Society of Rheology* 1972; 16(1): 99–127.

[11] Cross MM. Rheology of non-Newtonian fluids: a new flow equation for pseudoplastic sys-tems. *Journal of Colloid Science* 1965; 20(5): 417–437.

[12] Sochi T. Analytical solutions for the flow of Carreau and Cross fluids in circular pipes and thin slits. *Rheologica Acta* 2015; 54(8): 745–756.

[13] Moukhtari FE, Lecampion B. A semi-infinite hydraulic fracture driven by a shear thinning fluid. *Journal of Fluid Mechanics* 2018; 838: 573-605. http://dx.doi.org/10.1017/jfm.2017.900 doi: 10.1017/jfm.2017.900

[14] Wrobel M. On the application of simplified rheological models of fluid in the hydraulic fracture problems. *International Journal of Engineering Science* 2020; 150: 103275.

[15] Wrobel M, Mishuris G, Papanastasiou P. On the influence of fluid rheology on hydraulic fracture. *International Journal of Engineering Science* 2020; 158: 103426.

[16] Viesca RC, Garagash DI. Numerical methods for coupled fracture problems. *Journal of the Mechanics and Physics of Solids* 2018; 113: 13–34.

[17] Liu D, Lecampion B, Garagash D. Propagation of a fluid-driven fracture with fracture length dependent apparent toughness. *Engineering Fracture Me-chanics* 2019; 220. http://dx.doi.org/10.1016/j.engfracmech.2019.106616 doi: 10.1016/j.engfracmech.2019.106616

[18] Economides MJ, Nolte KG. *Reservoir Stimulation*. John Wiley & Sons . 2000.

[19] Garagash DI, Detournay E. The tip region of a fluid-driven fracture in an elastic medium. *ASME Journal of Applied Mechanics* 2000; 67: 183–192.

[20] Savitski A, Detournay E. Propagation of a penny-shaped fluid-driven fracture in an impermeable rock: asymptotic solutions. *International Journal of Solids and Structures* 2002; 39(26): 6311–6337. http://dx.doi.org/10.1016/S0020-7683(02)00492-4 doi: 10.1016/S0020-7683(02)00492-4

[21] Hills DA, Kelly PA, Dai DN, Korsunsky AM. *Solution of crack problems: the distributed dislocation technique.* 44 of *Solid Mechanics and its Applications.* Dordrecht: Kluwer Academic Publ. . 1996.

[22] Rice JR. Mathematical analysis in the mechanics of fracture. In: H. Liebowitz ., ed. *Fracture: An Advanced Treatise.* 2. 1968 (pp. 191–311).

[23] Szeri AZ. *Fluid Film Lubrication.* Cambridge University Press . 2010.

[24] Detournay E, Peirce AP. On the moving boundary conditions for a hydraulic fracture. *International Journal of Engineering Science* 2014; 84: 147–155.

[25] Garagash DI, Detournay E. Plane-strain propagation of a fluid-driven fracture: small toughness solution. *ASME Journal of Applied Mechanics* 2005; 72: 916–928.

[26] Garagash DI. Plane-strain propagation of a fluid-driven fracture during injection and shut-in: asymptotics of large toughness. *Engineering Fracture Mechanics* 2006; 73(4): 456–481. http://dx.doi.org/10.1016/j.engfracmech.2005.07.012 doi: 10.1016/j.engfracmech.2005.07.012

[27] Hu J, Garagash DI. Plane-strain propagation of a fluid-driven crack in a permeable rock with fracture toughness. *Journal of Engineering Mechanics* 2010; 136(9): 1152. http://dx.doi.org/10.1061/(ASCE)EM.1943-7889.0000169 doi: 10.1061/(ASCE)EM.1943-7889.0000169

[28] Erdogan F, Gupta GD, Cook T. Numerical solution of singular integral equations. In: Springer. 1973 (pp. 368–425).

[29] Guillot D, Dunand A. Rheological characterization of fracturing fluids by using laser anemometry. *Society of Petroleum Engineers Journal* 1985; 25(01): 39–45.